Stabilization and strengthening effects of functional groups in two-dimensional titanium carbide

Z. H. Fu,[1,2] Q. F. Zhang,[1,2,*] D. Legut,[3] C. Si,[1,2] T. C. Germann,[4] T. Lookman,[4] S. Y. Du,[5] J. S. Francisco,[6] and R. F. Zhang[1,2,†]

[1]*School of Materials Science and Engineering, Beihang University, Beijing 100191, People's Republic of China*

[2]*Center for Integrated Computational Engineering, International Research Institute for Multidisciplinary Science, Beihang University, Beijing 100191, People's Republic of China*

[3]*IT4Innovations Center, VSB-Technical University of Ostrava, CZ-70833 Ostrava, Czech Republic*

[4]*Theoretical Division, Los Alamos National Laboratory, Los Alamos, New Mexico 87545, USA*

[5]*Engineering Laboratory of Specialty Fibers and Nuclear Energy Materials, Ningbo Institute of Materials Technology and Engineering, Chinese Academy of Sciences, Ningbo, Zhejiang 315201, China*

[6]*Departments of Chemistry and Earth and Atmospheric Science, Purdue University, West Lafayette, Indiana 47906, USA*

(Received 15 March 2016; revised manuscript received 15 August 2016; published 2 September 2016)

Two-dimensional (2D) materials have attracted considerable interest due to their remarkable properties and potential applications for nanoelectronics, electrodes, energy storage devices, among others. However, many well-studied 2D materials lack appreciable conductivity and tunable mechanical strength, limiting their applications in flexible devices. Newly developed MXenes open up the opportunity to design novel flexible conductive electronic materials. Here, using density functional theory (DFT), we investigate systematically the effects of several functional groups on the stabilization, mechanical properties, and electronic structures of a representative MXene. It is found that oxygen possesses the largest adsorption energy as compared to other functional groups, indicating its good thermodynamic stabilization. In comparison with bare and other functionalized titanium carbides, the oxygen functionalized one exhibits the most superior ideal strength; however, the premature softening of the long-wave phonon modes might limit the intrinsic strength for $Ti_3C_2O_2$. Furthermore, the introduction of functional groups can induce a strong anisotropy under tensile loading. By analyzing the deformation paths and the electronic instability under various loadings, we demonstrate that the unique strengthening by oxygen functional groups is attributed to a significant charge transfer from inner bonds to outer surface ones after functionalization. Our results shed a novel view into exploring a variety of MXenes for their potential applications in flexible electronic and energy storage devices.

DOI: 10.1103/PhysRevB.94.104103

I. INTRODUCTION

Two-dimensional (2D) materials have attracted tremendous interest due to their unique character and intriguing properties that differ substantially from those of their three-dimensional (3D) counterparts. The first freestanding monolayer material is graphene, which was exfoliated or delaminated from graphite by Novoselov *et al.* [1] and drove the follow-up synthesis of a large number of 2D inorganic materials, including hexagonal boron nitrides [2], black phosphorous [3], transition metal dichalcogenides (TMDs) [4], metal oxides [5], hydroxides [6], and so on [7,8]. Since 2011, a new family of 2D transition metal carbides and nitrides, named MXenes, has received increasing attention owing to its excellent mechanical properties, metallic conductivity, and hydrophilic surfaces. This class of 2D materials was prepared by etching out the *A* layers from laminated *MAX* phases [9–11] (layered ternary carbides and nitrides, space group $P6_3/mmc$, where *M* represents an early transition metal, *A* denotes mainly the elements in group IIIA or IVA, and *X* can be either carbon or nitrogen [12,13]). Accompanied with the development of MXenes, researchers have increasingly unraveled their intriguing properties and potential applications [14–21] within the past few years, such as battery electrodes, electronics, photonics, chemical or temperature sensors, catalysis substrates, and energy storage materials.

Thus far, over 70 *MAX* phase materials have been reported, and more than 10 MXenes have been successfully synthesized, including Ti_3C_2 [9], Ti_2C [10], V_2C [11], Nb_2C [11], Ta_4C_3 [10], Nb_4C_3 [22], Mo_2C [23], $(Mo_2Ti)C_2$ [24], Zr_3C_2 [25], Ti_4N_3 [26], etc. Because different elements belonging to the same group of *M*, *A*, or *X* may occupy the same lattice positions in *MAX* phases, various new classes of *MAX* phases, such as $(Ti_{0.5}Nb_{0.5})_2AlC$ [27], $Ti_3(Al_{0.5}Si_{0.5})C_2$ [28], and $Ti_2Al(C_{0.5}N_{0.5})_2$ [29], have been accordingly synthesized. With these *MAX* phases as precursors, the relevant MXenes, like Ti_3CN [10], $(Ti_{0.5}Nb_{0.5})_2C$ [10], and $(V_{0.5}Cr_{0.5})_3C_2$ [10], developed the diversity of 2D MXenes.

The as-prepared MXenes are generally not standalone or bare from surface functionalization, especially when they are prepared by chemical exfoliation, and it has been demonstrated that full surface functionalization will be achieved in the experiment [30]. For convenience, we denote the surface functionalized MXenes with the general formula: $M_{n+1}X_nT_2$ where *T* stands for surface-terminating functional groups. For instance, Naguib *et al.* [9] have proposed an effective scheme to extract the Al layer from Ti_3AlC_2 phases by simply immersing Ti_3AlC_2 powders into hydrofluoric acid (HF). Under the solution environment of both HF and H_2O, the outer Ti layers of the bare Ti_3C_2 are not stable, and it is generally covered with various functional groups, such as O, F, and OH [31,32]. When the hydrochloric acid (HCl) and fluoride salt are used as the etching solution [15], another type of functional

*qianfan@buaa.edu.cn
†zrf@buaa.edu.cn

group, i.e. Cl, may also be expected to exist at the surface of 2D MXenes.

With these functional groups as a focus, many studies have shown that these functional groups play an important role on the properties of MXenes. Si *et al.* [33] found that a metal-to-insulator transition in functionalized Cr_2C is attributed to surface functional groups, like F, OH, H, or Cl, and it is accompanied by a ferromagnetic-antiferromagnetic transition due to localization of Cr d electrons. Xie and Kent [34] have studied the role of surface functional groups on the Li-ion energy storage capability of 2D transition metal carbides. They discovered that the functional oxygen groups possess the highest capability because oxygen-terminated MXene surfaces are able to absorb additional Li. In another paper, Eames and Islam [35] provided a similar conclusion that variation of surface functional groups can significantly affect the voltage and capability of MXenes, and the oxygen functionalized MXenes have the highest capability. On the contrary, Tang *et al.* [36] found that the bare Ti_3C_2 possesses a much lower barrier for Li diffusion and high Li storage capability as compared to the functionalized $Ti_3C_2T_2$ (with T = F or OH), and the surface functional groups, such as F or OH, can inhibit the transport of Li and decrease the Li storage capability. Shein and Ivanovskii [37] found that Ti_3C_2 and Ti_3N_2 are antiferromagnetic, and the magnetic moments are concentrated on the surface Ti. The inner Ti atoms and C/N atoms have little.

Besides the aforementioned electrochemical and magnetic properties, the mechanical strength and flexibility of MXenes have also attracted recent scientific interest. An early density functional theory (DFT) paper predicted that the functionalized $Ti_3C_2(OH)_2$ possesses a high elastic modulus along the basal plane ($c_{11} \approx 300$ GPa) [9], and a follow-up paper predicted that the elastic moduli c_{11} of various functionalized MXenes would be higher than that in the relevant *MAX* phases [38]. This can be attributed to the strengthening of the inside *M*-*X* bonds when the *A* atoms are removed and the valence charge density is more condensed inside the MXene layers [13]. Guo *et al.* [39] have extensively investigated the mechanical flexibility of a series of MXenes and found that the functionalized Ti_2CT_2 can sustain much larger strains than the bare Ti_2C, and the superior mechanical flexibility can be attributed to the slowdown effect of surface collapses, especially by functional groups [39]. The mechanical property of MXenes has also been used to strengthen some nanocomposites. Ling *et al.* [40] have shown that fabricated $Ti_3C_2T_x$/polymer composites possess high mechanical flexibility and electrical conductivities due to the strengthening and metallic conductivity of MXenes. The tensile strength of such composites is found to be significantly enhanced as compared to both pure $Ti_3C_2T_x$ and polymer alone.

Although much attention has been paid to the electrochemical and mechanical properties of bare and functionalized MXenes, there have been few studies on the stabilization and strengthening of the functionalized MXenes by various functional groups, which are critical to their unique electrochemical and mechanical properties and have extraordinary significance for their potential applications, such as flexible electronic and energy storage devices [41]. A number of investigations have been performed on the equilibrium bonding features, which is surely helpful for the microscopic insight into the reversible elastic properties of MXenes. However, little is known about the physical origin of stabilization and strengthening far from equilibrium by various functional groups, which hampers a suitable selection of functional groups for specific applications. In addition, modern theoretical methods to derive in-planar mechanical strength of a 2D MXene are controversial, and a rationalized justification needs to be further developed. It should be noted that the mechanical failure of a real material is generally determined by various defects, such as voids, dislocations, grain boundaries, cracks, etc. However, the ideal strength sets up the upper limit that a real material can attain, and it can be approached in some bulk materials [42] and 2D materials [43]. The calculation of ideal strength can also help the understanding of plastic deformation of a real material [44,45]. For instance, the measurement of the breaking strength of single-layer MoS_2 is quite close to ideal strength [43], and a recent study suggests that the failure of the strained graphene appears to be nearly ideal by means of nanoindentation [46]. Therefore, in this paper, we take $Ti_3C_2T_2$ with various T functional groups as the representatives of MXenes to first provide a comprehensive investigation into the effect of functional groups on the stabilization and mechanical strength by means of our implemented DFT-based scheme for mechanical tests. In order to reveal the origin of the strengthening effect induced by functional groups, we secondly performed a detailed analysis of the deformation paths, lattice instability modes, and electronic mechanism on both bare Ti_3C_2 and functionalized $Ti_3C_2O_2$. Our findings will broaden the potential applications of MXene materials, and simultaneously, provide an alternate pathway to strengthen 2D materials by tuning the functional species.

II. METHODOLOGY

Our spin-polarized DFT computations were performed using Vienna *Ab-initio* Simulation Package (VASP) [47] based on the projector augmented wave (PAW) method [48] employed to describe the electron-ion interaction with a plane wave cutoff energy of 600 eV. We used the local density approximation (LDA) [49] and the generalized gradient approximation (GGA) [50] exchange-correlation energy designed by Perdew, Burke, and Ernzerhof (PBE) [51]. Lattice parameters and atomic coordinates were optimized with an energy convergence of 10^{-6} eV/cell. The criterion for force convergence during the relaxation was 10^{-3} eV/Å. The dimension of the cell normal to the 2D layer was approximately 30 Å, and then the vacuum layer thickness was at least 18 Å. The mesh grid of k-points was adopted as $18 \times 18 \times 1$ for the primitive cell. The phonon calculations were performed by means of Phonopy code [52] based on the nonvanishing Hellman-Feynman forces within the harmonic approximation.

Since the antiferromagnetic ground state was reported to be energetically more favorable for bare Ti_3C_2 [37], we therefore checked the energy difference of its ferromagnetic and antiferromagnetic state to describe the spin-polarized state. Our results showed that the energy difference is about 0.043 eV/primitive cell, confirming that the antiferromagnetic state is energetically more favorable for the bare Ti_3C_2. It is observed that the bare Ti_3C_2 has an antiferromagnetic ground

state about 0.75 μ_B per surface Ti atom (the inner Ti atom shows nonmagnetic feature). While the $Ti_3C_2T_2$ (T = Cl, F, H, O, OH) have nonmagnetic ground states because of the surface passivation, in agreement with the previous results [36,37].

The adsorption energy (E_b) of functional groups T at the surface of a $M_{n+1}X_n$ was calculated based on the following equation:

$$E_b = \frac{\left(E_{M_{n+1}X_n} + 2E_T - E_{M_{n+1}X_nT_2}\right)}{2}, \quad (1)$$

where $E_{M_{n+1}X_n}$ is the total energy of the antiferromagnetic bare $M_{n+1}X_n$, E_T is the total energy of a free T atom or group, and $E_{M_{n+1}X_nT_2}$ is the total energy of the functionalized MXene with T as the functional groups [53].

To get the in-plane elastic constants, we applied a set of in-plane strains (ε_{xx} ε_{yy} ε_{xy}) ranging from -2 to $+2\%$ with an increment of 0.4%. The strain energy E_s is quadratically dependent on the applied strains and can be expressed as

$$E_s = a_1\varepsilon_{xx}^2 + a_2\varepsilon_{yy}^2 + a_3\varepsilon_{xx}\varepsilon_{yy} + a_4\varepsilon_{xy}^2, \quad (2)$$

where $E_s = E(\varepsilon) - E_0$, and $E(\varepsilon)$ and E_0 are the total energy of the strained and equilibrium system, respectively. Therefore, the in-plane planar elastic constants are derived as

$$c_{ij}^{2D} = \frac{1}{A_0}\left(\frac{\partial E_s^2}{\partial\varepsilon_i\partial\varepsilon_j}\right), \quad (3)$$

where $ij = xx, yy$, or xy, A_0 is the area of the simulation cell in the xy plane. The in-plane planar Young's and shear moduli, Poisson's ratio of a 2D system are derived from elastic constants as

$$E_x^{2D} = \frac{c_{11}^{2D}c_{22}^{2D} - c_{12}^{2D}c_{21}^{2D}}{c_{22}^{2D}}, \quad E_y^{2D} = \frac{c_{11}^{2D}c_{22}^{2D} - c_{12}^{2D}c_{21}^{2D}}{c_{11}^{2D}},$$
$$\nu_{xy}^{2D} = \frac{c_{21}^{2D}}{c_{22}^{2D}}, \quad \nu_{yx}^{2D} = \frac{c_{12}^{2D}}{c_{11}^{2D}}, \quad G_{xy}^{2D} = c_{66}^{2D}. \quad (4)$$

Note that the Young's modulus along a tension axis i can also be derived as $E_i = \frac{\sigma_i}{\varepsilon_i}$, and accordingly Poisson's ratio is expressed as $\nu_i = -\frac{d\varepsilon_j}{d\varepsilon_i}$, where ε_i and ε_j are the applied tensile strain in direction i and the response strain in direction j, respectively. Note that the method to derive an equivalent in-plane bulk elastic constant for MXenes was provided in the Supplemental Material [54], and the calculated values are listed in Table I. Since the 2D materials carry the in-plane loadings, the layer thickness will strongly influence the values of corresponding bulk elastic constants and moduli, as is discussed in previous studies [55]. When measuring effective thickness, van der Waals density functional (vdW-DF) of optB86b-vdW functional was performed [56,57].

TABLE I. The adsorption energies (E_b) for $Ti_3C_2T_2$. Energy unit is eV/atom or eV/molecule for OH.

	$Ti_3C_2Cl_2$	$Ti_3C_2F_2$	$Ti_3C_2H_2$	$Ti_3C_2O_2$	$Ti_3C_2(OH)_2$
I	4.566	6.358	3.065	7.057	5.077
II	4.830	6.720	3.426	7.771	5.305
III	4.700	6.538	3.249	7.413	5.195

Despite various definitions of effective layer thickness, a unified one is still much needed. It should be noticed that the approach to determine the effective thickness does not work when interlayer space is filled with something else or arbitrarily changed since, in that scenario, the bilayers are not at the equilibrium distance from the vdW force. In that case, however, a heterostructure model is generally relevant for both experimental and theoretical investigations [58]. Therefore, realistically, the in-plane planar elastic constants and moduli used in this paper do not rely on the choice of the thickness. The in-plane planar elastic constants and moduli can be obtained by rescaling the dimensional length Z of the simulated cell [59].

In our calculations of stress-strain relations of MXene nanosheets, both the in-plane uniaxial stress and the biaxial strain in tension are used to evaluate the mechanical response of various functionalized MXenes. The tensile strain is defined as $\varepsilon = \frac{a}{a_0}$, where a_0 and a are the equilibrium and strained lattice constant, respectively. To ensure that the MXene is under uniaxial stress, the geometry relaxation is performed for both the lattice basis vectors and the atomic coordinates by keeping the applied in-plane strain component fixed and relaxing the other in-plane strain component until their conjugate stress components, i.e., Hellmann–Feynman stresses, reach less than 0.1 GPa. In case of a 2D material, the dimensional length normal to the 2D layer is kept constant during the relaxation in order to keep a sufficient thickness of vacuum. Such a relaxation scheme is accomplished by slightly modifying the VASP code with specific constraints of strain components. To make sure that the strain path is continuous, the starting position at each strain step must be taken from the relaxed coordinates of the previous step. Because the crystal symmetry may be changed and the Brillouin zone significantly deformed at large strain, we adopted a high energy cutoff of 600 eV and verified the convergence of the stress-strain calculations with different k-point grids. A similar scheme for stress-strain calculation of 3D crystals has been described and thoroughly checked in our previous papers [60–62], to which we refer for further details. In case of 2D materials, two proposed schemes, i.e. in-plane planar stress and in-plane bulk stress, are generally used to account for the stress state. Therefore, in order to quantify the in-plane planar stress on the 2D MXene, the in-plane stress imposed on the simulated cell will be rescaled by Z to get an effective stress, where Z is the dimensional length of the simulated cell along the z direction. In a similar way to the definition of in-plane bulk elastic constants, we also calculated the in-plane bulk stress imposed on the simulated cell by Z/d_0 and provided the results in the Supplemental Material [54], where Z is the dimensional length of the simulated cell normal to the 2D plane and d_0 is the effective thickness of the 2D MXene. Here, the effective thickness is estimated based on the following procedure: (1) a bilayer model is constructed with a spacing determined via van der Waals force, (2) the layer thickness is defined as the distance between two equivalent carbon layers in the corresponding different MXene monolayer [55]. This procedure has already been used for the unique determination of the layer thickness of various 2D materials, such as graphene [63], molybdenum disulfide [64], and phosphorene [65].

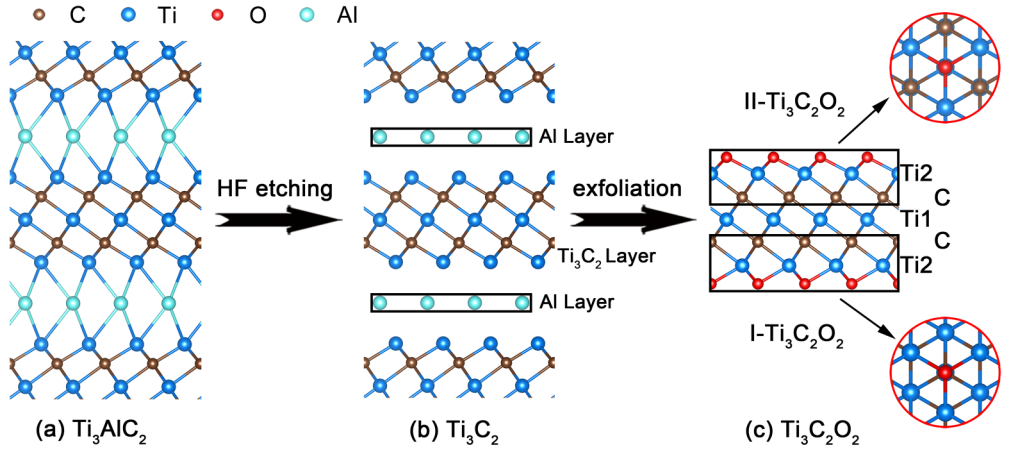

FIG. 1. Schematic of the exfoliation process for (c) MXenes from the corresponding (a) *MAX* phases. Red circles show two different configurations (I and II) of the surface group adsorption in vertical views.

III. RESULTS AND DISCUSSION

Figure 1 illustrates the exfoliation process for MXenes prepared from the corresponding *MAX* phases. First, the Ti_3AlC_2 phase [shown in Fig. 1(a)] is stirred in aqueous HF solutions for a given time, and then a centrifugation and filtration process is used to separate the 2D Ti_3C_2 [shown in Fig. 1(b)] from the supernatant solutions, and finally the Ti_3C_2 is cleaned with deionized water (DI) and sonication with methanol [9,13]. After elimination of the Al layers, the metallic Ti layers are exposed to air as terminated surfaces, with which the functional group T can make bonds and form a functionalized layered $Ti_3C_2T_2$ [shown in Fig. 1(c)]. At the terminated Ti_3C_2 surfaces, two types of hollow sites exist as indicated in Fig. 1(c): one at which a functional T group is aligned vertically to the inner C atom and bonded to three Ti2 atoms [i.e. Configuration I, the bottom surface shown in Fig. 1(c)]; and the other at which the functional T groups sit vertically on the top of Ti1 atoms and also bonded to three Ti2 atoms [i.e. Configuration II, the top surface shown in Fig. 1(c)]. When the functional groups are placed at different hollow sites on both top and bottom terminated surfaces, it is regarded as Configuration III. In this paper, both hollow sites are considered as the possible adsorption conformations of the functionalized groups.

Once the functional groups are placed at the hollow sites, a full DFT geometry relaxation is performed to find their most preferred positions. Since the adsorption features of Configuration III, such as bond lengths and adsorption energy, are always between configurations I and II, we shall focus mostly on the configurations I and II in the following sections, and the results for Configuration III are provided in the Supplemental Material [54]. Figure 2 shows the relaxed bond topology and lengths for bare Ti_3C_2 and functionalized $Ti_3C_2T_2$ in configurations I and II for T = Cl, F, H, O, and OH. It can be observed that the Ti2-C bond length [see Figs. 2(a) or 2(g)] inside the bare Ti_3C_2 nanosheet (2.065 Å) is slightly smaller than that of the bulk Ti_3AlC_2 phase (2.089 Å). When the functional F groups are introduced at the surfaces, the Ti2-C bonds inside $Ti_3C_2F_2$ are elongated to 2.100 and 2.078 Å for configurations I [see Fig. 2(c)] and II [see Fig. 2(i)], respectively. The Ti2-F bond length at the surface is 2.189 Å in Configuration I and 2.170 Å in Configuration II. In a similar manner, the functional OH group leads the Ti2-C and Ti2-O(H) bond lengths in $Ti_3C_2(OH)_2$ to be slightly larger (Ti2-C bond length: ∼2.107 Å in Configuration I [see Fig. 2(f)] and ∼2.087 Å in Configuration II [see Fig. 2(l)]; Ti2-O(H) bond length: ∼2.200 Å in Configuration I and ∼2.193 Å in Configuration II), in agreement with previous theoretical calculations [30,34,36]. Among the five types of functional groups, we notice that oxygen in Configuration II can induce the longest Ti2-C bond length (∼2.193 Å), the shortest Ti1-C bond length (∼2.159 Å), and the shortest Ti2-O bond length (∼1.981 Å), indicating a strengthening of inner Ti1-C bonds and a weakening of outer Ti2-C bonds as compared to other functional groups. Such bond modification may be linked to the significant thermodynamic stabilization and superior mechanical strength, as we will show in the latter sections.

We then investigate the thermodynamic stabilization of $Ti_3C_2T_2$ for various functional groups and adsorption sites by means of the calculated adsorption energies listed in Table I. It is found that, for all cases, the Configuration II absorption site is energetically more favored than the other sites, in

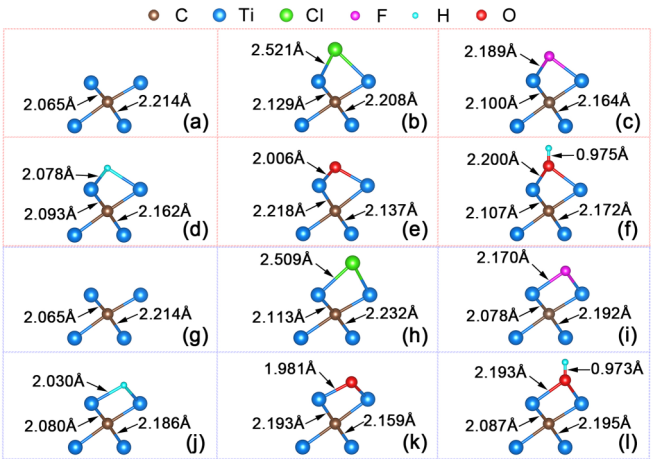

FIG. 2. The structural topology and bond lengths for (a) and (g) bare Ti_3C_2 and $Ti_3C_2T_2$ (T = Cl, F, H, O, OH) in (b)–(f) Configuration I and (h)–(l) Configuration II.

TABLE II. The in-plane planar elastic constants c_{11}^{2D} (unit: N/m), Young's moduli E_x^{2D} and E_y^{2D} (unit: N/m), Poisson's ratio v_{xy}^{2D} and v_{yx}^{2D} and in-plane planar shear moduli G_{xy}^{2D} (unit: N/m) of graphene, bare Ti_3C_2, and $Ti_3C_2T_2$ compared with previous calculations and available experimental measurement. The values in brackets are the in-plane bulk elastic constants c_{11} (unit: GPa), Young's moduli E_x and E_y (unit: GPa), Poisson's ratio ν_{xy} and ν_{yx} and in-plane bulk shear moduli G_{xy} (unit: GPa), respectively. Note the values of ν_{xy} and ν_{yx} are equal to v_{xy}^{2D} and v_{yx}^{2D}. Note that the meanings of the abbreviations listed in the table are: DFT: The density functional theory, VASP: Vienna *Ab-initio* Simulation Package, force field: The in-plane force field methods performed by Quantum-Espresso computer code, ABINIT: The ABINIT code, AIMPRO: The AIMPRO code, Exp.: Experiment, CASTEP: Cambridge Sequential Total Energy Package.

	$c_{11}^{2D}(c_{11})$	$E_x^{2D}(E_x)$	$E_y^{2D}(E_y)$	v_{xy}^{2D} (ν_{xy})	$v_{yx}^{2D}(\nu_{yx})$	$G_{xy}^{2D}(G_{xy})$	
Graphene	339 (1011)	321 (957)	321 (958)	0.230	0.230	133 (397)	PAW-PBE (this paper)
	350 (1045)	330 (984)	330 (984)	0.243	0.243	139 (414)	PAW-LDA (this paper)
	358			0.169			DFT-VASP[a]
	361	350		0.184			DFT-VASP[b]
		320		0.220			DFT force field[c]
		336		0.170			DFT-ABINIT[d]
		350		0.200			DFT-AIMPRO[e]
		330 ± 15					Exp.[f]
Bare	241 (330)	228 (313)	227 (312)	0.227	0.226	103 (141)	PAW-PBE (this paper)
	(523)						CASTEP[g]
Cl	300 (271)	281 (253)	283 (255)	0.253	0.255	112 (101)	PAW-PBE (this paper)
F	316 (334)	295 (312)	293 (309)	0.260	0.258	119 (125)	
H	316 (419)	302 (392)	300 (398)	0.209	0.208	124 (165)	
O	379 (402)	347 (368)	347 (369)	0.291	0.291	135 (144)	
OH	282 (290)	256 (262)	260 (267)	0.304	0.309	101 (104)	

[a]Ref. [69].
[b]Ref. [68].
[c]Ref. [70].
[d]Ref. [71].
[e]Ref. [72].
[f]Ref. [46].
[g]Ref. [38].

agreement with previous results [34,36,66]. Among all the functionalized $Ti_3C_2T_2$, $Ti_3C_2O_2$ (7.771 eV) possesses the maximum adsorption energy, which is followed by $Ti_3C_2F_2$ (6.720 eV), $Ti_3C_2(OH)_2$ (5.305 eV), $Ti_3C_2Cl_2$ (4.830 eV), and $Ti_3C_2H_2$ (3.426 eV). After an analysis of bond lengths and adsorption energies, we suppose that there is an intrinsic connection between them: a shorter length of Ti2-T bonds corresponds to a larger adsorption energy of the T group, indicating a better stabilization induced by the functional group. These results suggest that all the functional groups tend to be attracted at the Configuration II hollow sites.

We now turn to investigate the mechanical properties of various functionalized $Ti_3C_2T_2$. For a validation, we have firstly calculated the mechanical property of parent Ti_3AlC_2 and compared with the previous values. Our results produce the lattice parameters of Ti_3AlC_2: $a = 3.082$ Å, $c = 18.641$ Å, and the elastic constant of c_{11}: 367 GPa, being in excellent agreement with previous values (3.0816 Å [34], 3.0824 Å [37], 368 GPa [38]). In addition, using the graphene as a further validator, we have checked our calculation scheme on the elastic properties by means of both PAW-LDA and PAW-PBE potentials. Our calculated C-C bond length in graphene is about 1.424 Å (PAW-PBE) and 1.412 Å (PAW-LDA), being very close to that in the graphite (1.418 Å by PAW-PBE) and in good agreement with previous results [67,68]. Afterwards, the same scheme is used to calculate the in-plane planar elastic constants, Poisson's ratio, in-plane planar Young's moduli, and in-plane planar shear moduli of both bare Ti_3C_2 and $Ti_3C_2T_2$ and compared with those of graphene in Table II [38,46,68–72]. Our results indicate clearly that all the functionalized $Ti_3C_2T_2$ (256–347 N/m) in this paper possess relatively higher in-plane planar Young's moduli than the bare Ti_3C_2 (228 N/m), with the highest value found for $Ti_3C_2O_2$ (347 N/m). For the comparison of the in-plane bulk Young's moduli, we can find a similar conclusion (for the definition and deduction, see the Supplemental Material [54]). However, $Ti_3C_2H_2$ performs with excellent properties because of a reduced effective thickness, which can be attributed to the smaller radius of the H atom (see Fig. S2 and Table S1 in the Supplemental Material [54]). Similarly, the second largest Poisson's ratio is also observed for oxygen functionalized $Ti_3C_2O_2$ (0.291), which is about 66% higher than the bare Ti_3C_2. It is generally believed that a higher Poisson's ratio indicates better mechanical ductility and flexibility. Such a hypothesis is in agreement with the most recent studies by Guo *et al.* for another type of MXene Ti_2CT_2 [39]. It should be noted that our derived elastic property differs from the previous values [38] due to different layer thickness defined for stress quantification. To account for the in-plane elastic anisotropy, we use the ratio of two in-plane planar Young's moduli, i.e. $A = \frac{E_x^{2D}}{E_y^{2D}}$, as an in-plane anisotropy index. The calculated values of A reveal that both bare Ti_3C_2 and functionalized $Ti_3C_2T_2$ exhibit good isotropy ($A \approx 1$). However, as will be shown in the next section, elastic isotropy cannot guarantee isotropic in-plane mechanical strengths. Since the in-plane shear modulus provides a resistance to shape change of a

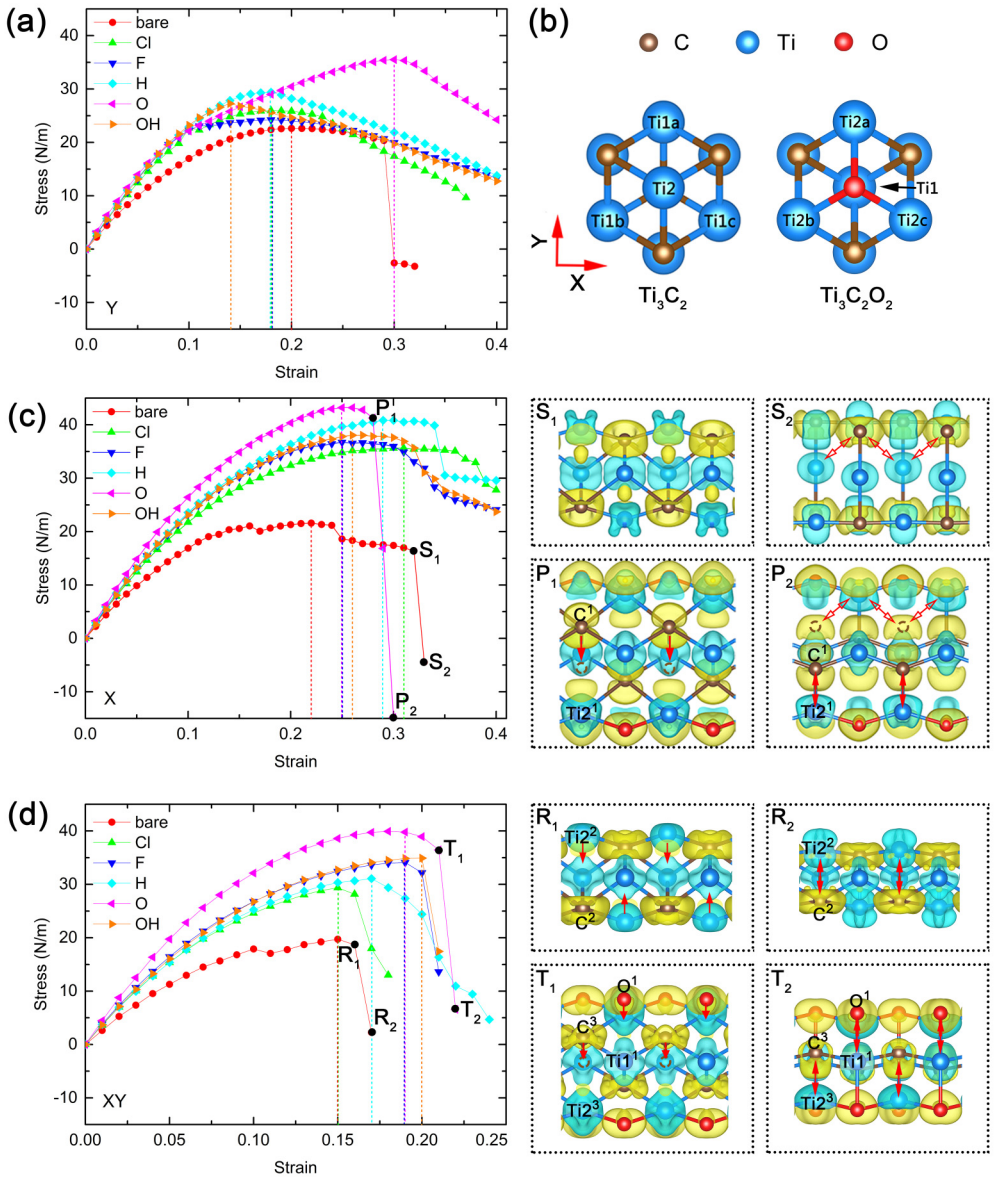

FIG. 3. (a) The stress-strain curves in the uniaxial tension Y direction. (b) The schematic of tensile directions and stacking orders for Ti_3C_2 and $Ti_3C_2O_2$. (c) The stress-strain curves in the uniaxial tension X direction, and the VCDDs of S_1 and S_2 for Ti_3C_2 and P_1 and P_2 for $Ti_3C_2O_2$. (d) The stress-strain curves in biaxial tension, and the VCDDs of R_1 and R_2 for Ti_3C_2 and T_1 and T_2 for $Ti_3C_2O_2$. All the vertical lines mention the maximum stress values. The isosurface maps of the VCDD correspond to ± 0.012 electrons/Bohr^3.

2D material, our calculated shear moduli indicate that the functionalized $Ti_3C_2T_2$ possesses a higher in-plane stiffness as compared to bare Ti_3C_2.

An elastic modulus describes a reversible response of a material to a small lattice distortion around equilibrium, while an ideal strength gives an upper limit of irreversible lattice resistance to a large strain, which a material can sustain. Figure 3 shows the calculated stress-strain curves under uniaxial stress and biaxial strain in tension. It can be seen that all functionalized $Ti_3C_2T_2$ (24.2–43.2 N/m) we studied possess much higher strength than the bare Ti_3C_2 (19.7–22.6 N/m) for all three deformation modes. Among the five functional groups, the most profound enhancement of strength is found for the oxygen functionalized $Ti_3C_2O_2$ (i.e. 35.5 N/m for $Ti_3C_2O_2$ vs 22.6 N/m for Ti_3C_2 under uniaxial tension along the Y direction, 43.2 N/m for $Ti_3C_2O_2$ vs 21.6 N/m for Ti_3C_2 under uniaxial tension along the X direction, 39.9 N/m for $Ti_3C_2O_2$ vs 19.7 N/m for Ti_3C_2 under biaxial tension). For the comparison of the in-plane bulk stress-strain curve in different directions, we can obtain a similar conclusion (see Fig. S3 in the Supplemental Material [54]). An exception of the curve is the X direction tension, where the smaller effective thickness provides $Ti_3C_2H_2$ a greater strength.

In case of uniaxial tension along the X and Y directions, a nearly isotropic in-plane planar strength is shown for bare Ti_3C_2, whereas a strong anisotropy of in-plane planar strength is found for functionalized $Ti_3C_2T_2$, which can be attributed to the nonequivalent feature of in-plane bond topology as seen from the top view shown on the right side of Fig. 3(b). From the top view of the functionalized $Ti_3C_2T_2$, we can hypothesize

that the T-Ti2b and T-Ti2c bonds will carry the resistance to the tension loading along the X direction, while the T-Ti2a bonds will be stressed during tension along the Y direction, being balanced by the stress imposed on both T-Ti2b and T-Ti2c bonds. Such a structural feature is responsible for the anisotropic strength of $Ti_3C_2T_2$ and also contributes to the different deformation path, as will be discussed below. In case of tensile loading along the X direction, a phase transformation mode is responsible for the lowering of the $Ti_3C_2O_2$ stress-strain curve, while a simple bond instability mode is seen for $Ti_3C_2Cl_2$, $Ti_3C_2H_2$, $Ti_3C_2F_2$, and $Ti_3C_2(OH)_2$, setting an upper limit of tensile stress. When the loading is along the Y direction, the simple bond instability controls the maximum tensile strength for all functionalized $Ti_3C_2T_2$, but the biaxial tension will cause the failure of bare Ti_3C_2 and $Ti_3C_2T_2$ to be accompanied by phase transformation, which induce the functional T layers and C layers to be squeezed close to Ti2 and Ti1 layers, respectively.

To further understand the deformation paths of both bare Ti_3C_2 and functionalized $Ti_3C_2T_2$ in different loadings, the change of bond lengths and valence charge density differences (VCDDs) are presented in Fig. 3. (The VCDD is calculated by the difference between the total valence charge density of the MXene minus the superposition of the valence charge densities of neutral atoms [60].) A positive value (yellow color) means an accumulation of the negative charge (bond strengthening), while a negative value (cyan color) means a depletion of charges as compared to neutral atoms (bond weakening). Because the oxygen group shows the most profound strengthening among all the functional groups [see Figs. 3(a), 3(c), and 3(d)], we shall focus on the deformation mechanism of bare Ti_3C_2 and the functionalized $Ti_3C_2O_2$ as an illustration for a comparative study.

In the case of bare Ti_3C_2, the bond weakening first appears between the inner Ti1-C bonds, which increase from 2.214 Å (equilibrium position) to 2.699 Å [at S_1 point in Fig. 3(c)]. After lattice instability, a phase transformation appears with the outer Ti2 layer becoming nearly parallel to the inner C layer [see the VCDD marked by S_1 and S_2 on the right side of Fig. 3(c)]. Such a change of bond topology induces a redistribution of VCDD between Ti1-C bonds, confirming that the bond instability of Ti_3C_2 is mainly due to the weakening of the inner Ti1-C bonds. In comparison, the functional oxygen group can effectively hinder the bond weakening of the inner Ti1-C bonds by forming outer Ti2-O bonds at the surface [see the VCDD marked by P_1 and P_2 on the right side of Fig. 3(c)]. During the lattice instability, the bond lengths change slightly from 2.137 to 2.360 Å for Ti1-C bonds and from 1.981 to 2.105 Å for Ti2-O bonds, respectively. Although the bond instability occurs also between Ti2-C bonds, changing from 2.193 to 2.703 Å, a much higher strength is required as compared to bare Ti_3C_2. After lattice instability, the positive value of VCDD becomes more profound between $Ti2^1$ and C^1 atoms, confirming the formation of new bonds [see P_2 on the right side of Fig. 3(c)]. The O atomic layers and C atomic layers move closer to Ti2 and Ti1 atomic layers, respectively, indicating the formation of a novel metastable structure.

We now turn to investigate the deformation paths for bare Ti_3C_2 and the functionalized $Ti_3C_2O_2$ under the biaxial tensile loadings. It is seen from Fig. 3(d) that a distinct change of layer thickness appears because of the Poisson contraction. In case of bare Ti_3C_2 [see the VCDD marked by R_1 and R_2 on the right side of Fig. 3(d)], we discover that the outer Ti atomic layers move closer to the inner C atomic layers during biaxial tensions. After lattice instability, the lengths of the Ti1-C and Ti2-C bonds change from 2.444 to 2.330 Å and from 2.165 to 2.211 Å, respectively. Simultaneously, the distance between the top $Ti2^2$ layers and the bottom C^2 layers decreases greatly from 3.186 to 2.162 Å, to be accompanied with the formation of new $Ti2^2$-C^2 bonds. In comparison, the functional oxygen group will change the deformation path of $Ti_3C_2O_2$ [see the VCDD marked by T_1 and T_2 on the right side of Fig. 3(d)]. Instead of the shrinkage of inner Ti1 atomic layers, the outer O and the inner C atomic layers squeeze inwards. The atomic distance between O^1 and $Ti1^1$ changes from 2.781 to 2.165 Å, and meanwhile, the distance between $T2^3$ and C^3 changes from 3.217 to 2.107 Å, suggesting the formation of new O^1-$Ti1^1$ and $T2^3$-C^3 bonds. During this process, the Ti1-C and Ti2-C bonds do not change so much, which can be confirmed by the VCDD isosurfaces.

TABLE III. Bader charges for bare Ti_3C_2 and $Ti_3C_2T_2$, unit is electron.

	Bare	Cl	F	H	O	OH
Ti1	+1.43	+1.43	+1.42	+1.44	+1.5	+1.43
Ti2	+1.05	+1.49	+1.59	+1.43	+1.71	+1.57
C	–1.76	–1.62	–1.6	–1.58	–1.48	–1.6
T		–0.57	–0.7	–0.56	–0.98	–0.68

To reveal the physical origin of the unique stabilization and mechanical strength, we have calculated the Bader charges of each functionalized $Ti_3C_2T_2$ and compared them to that of bare Ti_3C_2. Table III lists the calculated Bader charges on each atom. When the functional groups are placed at the hollow sites, the Bader charges on Ti2 atoms increase significantly, i.e. +1.43 for $Ti_3C_2H_2$, +1.49 for $Ti_3C_2Cl_2$, +1.57 for $Ti_3C_2(OH)_2$, +1.59 for $Ti_3C_2F_2$, and +1.71 for $Ti_3C_2O_2$ vs +1.05 for bare Ti_3C_2. It can be found that the Bader charges on Ti2 atoms in $Ti_3C_2O_2$ provide the most positive values as compared to the other four functional groups. Meanwhile, the Bader charges on Ti1 atoms in $Ti_3C_2O_2$ have the most positive values, and the Bader charges on C atoms in $Ti_3C_2O_2$ have the lowest value as compared to other functional groups, suggesting that oxygen is the best functional group to gain more charges from the inner Ti atoms, which provides an electronic basis for why $Ti_3C_2O_2$ has the best thermodynamic stabilization, i.e. highest adsorption energy. The charge distribution in $Ti_3C_2O_2$ weakens the outer Ti2-C bonds and forms relatively strong Ti2-O bonds compared to that of other $Ti_3C_2T_2$ and bare Ti_3C_2. Compared to $Ti_3C_2O_2$, other $Ti_3C_2T_2$ form relatively weaker Ti2-T bonds due to the smaller charge migration. So in the tensile direction X, bare Ti_3C_2, $Ti_3C_2O_2$, and other $Ti_3C_2T_2$ experience a different deformation mode. In the tensile direction Y, strong Ti2-O bonds provide pretty high strength. We have further investigated the connection between the electronegativity of the adsorbed species and the bond strength (or adsorption energies). Among the five adsorbed species, the smallest

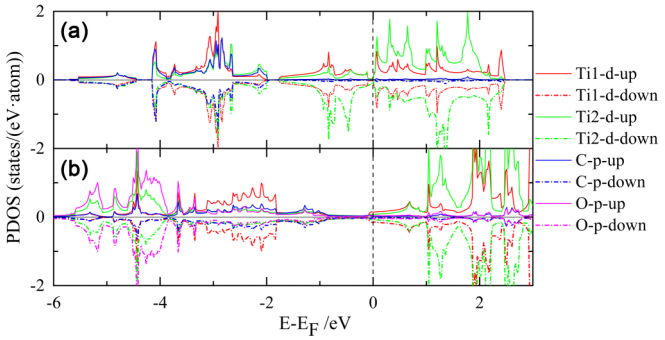

FIG. 4. Electronic partial density of states (PDOS) for (a) bare Ti_3C_2 and (b) $Ti_3C_2O_2$.

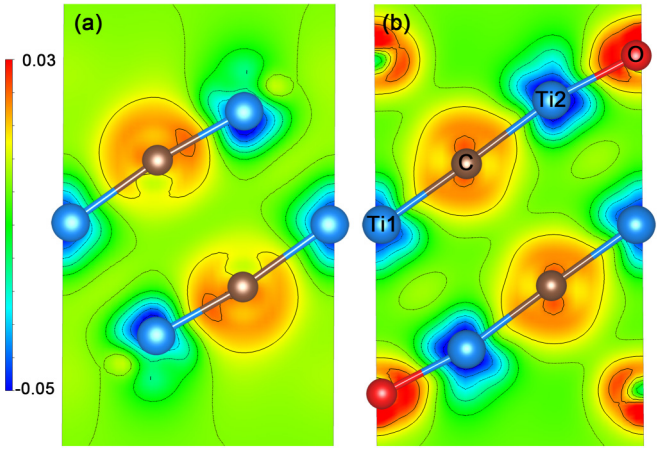

FIG. 5. Cross-sectional plots of the VCDDs in the vertical plane including the Ti2-C bond for (a) bare Ti_3C_2 and (b) $Ti_3C_2O_2$. The thick solid and thin dotted contours represent positive and negative values, respectively. Charge unit is electron/Bohr^3.

adsorption energy of hydrogen corresponds to its lowest electronegativity, whereas although fluorine has the maximum electronegativity, its adsorption energy (6.720 eV/atom) is about 1 eV/atom lower than that of oxygen (7.771 eV/atom), suggesting that a higher electronegativity does not always guarantee a stronger bonding strength.

Although ideal strength may provide the intrinsic bond strength and detailed deformation paths, it cannot guarantee a dynamic stability upon straining before lattice instability occurs. Therefore, we next investigate the dynamic stability for the strained bare Ti_3C_2 and the oxygen functionalized $Ti_3C_2O_2$ along the three strain modes. It is found that the soft phonon modes highlighted in Figs. S4 and S5 in the Supplemental Material [54] occur around the Γ point, indicating the softening of the long-wave phonon modes, i.e. elastic instability [73] before the peak stresses, except for the biaxial tension for the bare Ti_3C_2, and it occurs just near the critical stresses for bare Ti_3C_2 along X and Y tension loadings. In the case of the oxygen functionalized $Ti_3C_2O_2$, the critical strains (stresses) for phonon softening are 0.10 (stress = ~26.4 N/m), 0.09 (stress = ~20.9 N/m), 0.06 (stress = ~22.8 N/m) along X, Y, and XY tension loadings, respectively (see Figs. S4 and S5 in the Supplemental Material [54]). Comparing with the in-plane planar stress, the critical stresses for phonon softening of $Ti_3C_2O_2$ are slightly higher than those of the bare Ti_3C_2 except for the Y tension. Note that the phonon softening are generally observed in many 2D materials, including graphene [74], BN [75], MoS_2 [64], etc. The phonon calculations are generally accessible for 2D materials within harmonic approximation, which however does not account for an anharmonic stabilization that is found to play an important role on stabilization at finite temperature in some cases. For example, the critical strain for phonon softening is found much lower than that experimentally identified lattice instability for graphene, and the origin might be attributed to an anharmonic stabilization [74]. In view of these facts, both lattice instabilities and phonon softening would benefit from the understanding of the strengthening effect of MXenes.

Figure 4 compares the calculated electronic partial density of states (PDOS) for bare Ti_3C_2 and $Ti_3C_2O_2$. Both bare Ti_3C_2 and functionalized $Ti_3C_2O_2$ are metallic conductors, in agreement with previous results [36,37]. Compared to the PDOS of parent Ti_3AlC_2 (see Fig. S6 in the Supplemental Material [54]), there are relatively large values of DOS around the Fermi level in the bare Ti_3C_2, which is mainly attributed to the d orbitals of Ti atoms, and the Ti1 atom is likely to be nonmagnetic because of symmetry distribution of spin-up and spin-down in PDOS. The functional oxygen decreases the DOS at the Fermi level (the DOS of Ti2-d orbitals decreases more), and it can be clearly seen that a pseudogap forms nearby [76]. A similar phenomenon has also been reported on the Ti_2C system [34,37]. The DOS at the Fermi level is mostly attributed to the d orbitals of Ti1 and relatively less attributed to the ones of Ti2. It indicates a strengthening for $Ti_3C_2O_2$ by the unpaired electrons at surface. Such electronic characteristics can also be used to explain the aforementioned unique mechanical strength of $Ti_3C_2O_2$. In addition, the peaks of the antibonding state above the Fermi level for functionalized $Ti_3C_2O_2$ move upward to the high energy level. This provides another physical understanding why $Ti_3C_2O_2$ is the strongest one under tension along the Y direction.

Figure 5 shows the cross-sectional plots of the valence charge-density differences between Ti2-C bonds. It can be discovered that the shorter Ti2-C bonds in bare Ti_3C_2 correspond to a higher accumulation of valence charge between them as compared to $Ti_3C_2O_2$, providing further evidence that the functional oxygen induces a charge transfer from inner Ti-C to outer Ti-O bonds. Such charge migration can decrease the charge accumulation between Ti2-C bonds, which is responsible for the instability mode in uniaxial and biaxial tension.

IV. CONCLUSIONS

In summary, we have systematically investigated the effect of various functional groups on the stabilization, mechanical properties, deformation paths, and electronic origin of a representative MXene, Ti_3C_2. Among the five functional groups we considered, F, Cl, OH, H, and O, the oxygen functionalized $Ti_3C_2O_2$ possesses the largest adsorption energy, the highest in-plane planar elastic modulus, and the greatest enhancement of strength. By analyzing the deformation paths under various tensile loadings, we infer that the phase transformation and simple bond instability determines the different stress-strain

responses, depending on the types of functional groups and loading modes. The phonon softening upon straining is found for both bare Ti_3C_2 and oxygen functionalized $Ti_3C_2O_2$ before maximum stress peaks, which might intrinsically limit their strengths. The in-depth comparison of electronic structure between bare Ti_3C_2 and oxygen functionalized $Ti_3C_2O_2$ suggests that the significant stabilization and strengthening by oxygen functional groups is mainly attributed to the charge transfer from inner Ti-C bonds to the outer Ti-O surfaces ones, which eventually hinder the irreversible deformation and require a high critical stress for lattice failure. Our results provide a fundamental basis for the exploration of a variety of functionalized MXenes for their possible applications in flexible electronic and energy storage devices.

ACKNOWLEDGMENTS

Z.H.F. and R.F.Z. are supported by the Fundamental Research Funds for the Central Universities, National Natural Science Foundation of China (Grants No. 51471018 and No. 51672015), and National Thousand Young Talents Program of China. Q.F.Z. is supported by National Natural Science Foundation of China (Grant No. 11404017), Technology Foundation for Selected Overseas Chinese Scholar, Ministry of Human Resources and Social Security of China, and the Program for New Century Excellent Talents in University (NCET-12-0033). D.L. acknowledges IT4Innovations Centre of Excellence project (CZ.1.05/1.1.00/02.0070), funded by the European Regional Development Fund and the national budget of the Czech Republic via the Research and Development for Innovations Operational Programme, as well as Czech Ministry of Education, Youth and Sports via the project Large Research, Development, and Innovations Infrastructures (LM2011033). We appreciate the support from the key technology of nuclear energy, 2014, CAS Interdisciplinary Innovation Team and ITaP at Purdue University for computing resources. We would also like to thank G. Kresse for valuable advice for the application of VASP.

[1] K. S. Novoselov, A. K. Geim, S. V. Morozov, D. Jiang, Y. Zhang, S. V. Dubonos, I. V. Grigorieva, and A. A. Firsov, Science **306**, 666 (2004).
[2] D. Pacile, J. C. Meyer, C. O. Girit, and A. Zettl, Appl. Phys. Lett. **92**, 133107 (2008).
[3] L. Li, Y. Yu, G. J. Ye, Q. Ge, X. Ou, H. Wu, D. Feng, X. H. Chen, and Y. Zhang, Nat. Nanotechnol. **9**, 372 (2014).
[4] J. N. Coleman, M. Lotya, A. O'Neill, S. D. Bergin, P. J. King, U. Khan, K. Young, A. Gaucher, S. De, R. J. Smith, I. V. Shvets, S. K. Arora, G. Stanton, H.-Y. Kim, K. Lee, G. T. Kim, G. S. Duesberg, T. Hallam, J. J. Boland, J. J. Wang *et al.*, Science **331**, 568 (2011).
[5] K. S. Novoselov, D. Jiang, F. Schedin, and T. J. Booth, Proc. Natl. Acad. Sci. USA **102**, 10451 (2005).
[6] R. Ma and T. Sasaki, Adv. Mater. **22**, 5082 (2010).
[7] M. Q. Zhao, M. Sedran, Z. Ling, M. R. Lukatskaya, O. Mashtalir, M. Ghidiu, B. Dyatkin, D. J. Tallman, T. Djenizian, and M. W. Barsoum, Angew. Chem.-Int. Edit. **54**, 4810 (2015).
[8] V. Nicolosi, M. Chhowalla, M. G. Kanatzidis, M. S. Strano, and J. N. Coleman, Science **340**, 1226419 (2013).
[9] M. Naguib, M. Kurtoglu, V. Presser, J. Lu, J. Niu, M. Heon, L. Hultman, Y. Gogotsi, and M. W. Barsoum, Adv. Mater. **23**, 4248 (2011).
[10] M. Naguib, O. Mashtalir, J. Carle, V. Presser, J. Lu, L. Hultman, Y. Gogotsi, and M. W. Barsoum, ACS Nano **6**, 1322 (2012).
[11] M. Naguib, J. Halim, J. Lu, K. M. Cook, L. Hultman, Y. Gogotsi, and M. W. Barsoum, J. Am. Chem. Soc. **135**, 15966 (2013).
[12] M. W. Barsoum, Prog. Solid State Ch. **28**, 201 (2000).
[13] M. Naguib, V. N. Mochalin, M. W. Barsoum, and Y. Gogotsi, Adv. Mater. **26**, 992 (2014).
[14] M. R. Lukatskaya, O. Mashtalir, C. E. Ren, Y. Dall'Agnese, P. Rozier, P. L. Taberna, M. Naguib, P. Simon, M. W. Barsoum, and Y. Gogotsi, Science **341**, 1502 (2013).
[15] M. Ghidiu, M. R. Lukatskaya, M. Q. Zhao, Y. Gogotsi, and M. W. Barsoum, Nature **516**, 78 (2014).
[16] X. Xie, Y. Xue, L. Li, S. Chen, Y. Nie, W. Ding, and Z. Wei, Nanoscale **6**, 11035 (2014).
[17] C. Xu, L. Wang, Z. Liu, L. Chen, J. Guo, N. Kang, X. L. Ma, H. M. Cheng, and W. Ren, Nat. Mater. **14**, 1135 (2015).
[18] M. Q. Zhao, C. E. Ren, Z. Ling, M. R. Lukatskaya, C. Zhang, K. L. Van Aken, M. W. Barsoum, and Y. Gogotsi, Adv. Mater. **27**, 339 (2015).
[19] S. J. Kim, M. Naguib, M. Q. Zhao, C. F. Zhang, H. T. Jung, M. W. Barsoum, and Y. Gogotsi, Electrochim. Acta **163**, 246 (2015).
[20] M. Naguib, J. Come, B. Dyatkin, V. Presser, P. L. Taberna, P. Simon, M. W. Barsoum, and Y. Gogotsi, Electrochem. Commun. **16**, 61 (2012).
[21] Y. Gao, D. Ma, G. Hu, P. Zhai, X. Bao, B. Zhu, B. Zhang, and D. S. Su, Angew. Chem.-Int. Edit. **50**, 10236 (2011).
[22] M. Ghidiu, M. Naguib, C. Shi, O. Mashtalir, L. M. Pan, B. Zhang, J. Yang, Y. Gogotsi, S. J. Billinge, and M. W. Barsoum, Chem. Commun. **50**, 9517 (2014).
[23] R. Meshkian, L.-Å. Näslund, J. Halim, J. Lu, M. W. Barsoum, and J. Rosen, Scr. Mater. **108**, 147 (2015).
[24] B. Anasori, Y. Xie, M. Beidaghi, J. Lu, B. C. Hosler, L. Hultman, P. R. Kent, Y. Gogotsi, and M. W. Barsoum, ACS Nano **9**, 9507 (2015).
[25] J. Zhou, X. Zha, F. Y. Chen, Q. Ye, P. Eklund, S. Du, and Q. Huang, Angew. Chem.-Int. Edit. **128**, 5092 (2016).
[26] P. Urbankowski, B. Anasori, T. Makaryan, D. Er, S. Kota, P. L. Walsh, M. Zhao, V. B. Shenoy, M. W. Barsoum, and Y. Gogotsi, Nanoscale **8**, 11385 (2016).
[27] I. Salama, T. El-Raghy, and M. W. Barsoum, J. Alloy. Compd. **347**, 271 (2002).
[28] H. B. Zhang, Y. C. Zhou, Y. W. Bao, M. S. Li, and J. Y. Wang, J. Eur. Ceram. Soc. **26**, 2373 (2006).
[29] M. W. Barsoum, T. El-Raghy, and M. Ali, Metall. Mater. Trans. A **31**, 1857 (2000).

[30] M. Khazaei, M. Arai, T. Sasaki, C. Y. Chung, N. S. Venkataramanan, M. Estili, Y. Sakka, and Y. Kawazoe, Adv. Funct. Mater. **23**, 2185 (2013).
[31] Q. Peng, J. Guo, Q. Zhang, J. Xiang, B. Liu, A. Zhou, R. Liu, and Y. Tian, J. Am. Chem. Soc. **136**, 4113 (2014).
[32] Y. Xie, M. Naguib, V. N. Mochalin, M. W. Barsoum, Y. Gogotsi, X. Q. Yu, K. W. Nam, X. Q. Yang, A. I. Kolesnikov, and P. R. C. Kent, J. Am. Chem. Soc. **136**, 6385 (2014).
[33] C. Si, J. Zhou, and Z. Sun, ACS Appl. Mater. Inter. **7**, 17510 (2015).
[34] Y. Xie and P. R. C. Kent, Phys. Rev. B **87**, 235441 (2013).
[35] C. Eames and M. S. Islam, J. Am. Chem. Soc. **136**, 16270 (2014).
[36] Q. Tang, Z. Zhou, and P. Shen, J. Am. Chem. Soc. **134**, 16909 (2012).
[37] I. R. Shein and A. L. Ivanovskii, Comp. Mater. Sci. **65**, 104 (2012).
[38] M. Kurtoglu, M. Naguib, Y. Gogotsi, and M. W. Barsoum, MRS Commun. **2**, 133 (2012).
[39] Z. Guo, J. Zhou, C. Si, and Z. Sun, Phys. Chem. Chem. Phys. **17**, 15348 (2015).
[40] Z. Ling, C. E. Ren, M.-Q. Zhao, J. Yang, J. M. Giammarco, J. Qiu, M. W. Barsoum, and Y. Gogotsi, Proc. Natl. Acad. Sci. USA **111**, 16676 (2014).
[41] X. Wang, X. Lu, B. Liu, D. Chen, Y. Tong, and G. Shen, Adv. Mater. **26**, 4763 (2014).
[42] W. Z. Han, L. Huang, S. Ogata, H. Kimizuka, Z. C. Yang, C. Weinberger, Q. J. Li, B. Y. Liu, X. X. Zhang, and J. Li, Adv. Mater. **27**, 3385 (2015).
[43] S. Bertolazzi, J. Brivio, and A. Kis, ACS Nano **5**, 9703 (2011).
[44] R. F. Zhang, X. D. Wen, D. Legut, Z. H. Fu, S. Veprek, E. Zurek, and H. K. Mao, Sci. Rep. **6**, 23088 (2016).
[45] Z. J. He, Z. H. Fu, D. Legut, X. H. Yu, Q. F. Zhang, V. I. Ivashchenko, S. Veprek, and R. F. Zhang, Phys. Rev. B **93**, 184104 (2016).
[46] C. Lee, X. Wei, J. W. Kysar, and J. Hone, Science **321**, 385 (2008).
[47] G. Kresse and J. Furthmüller, Phys. Rev. B **54**, 11169 (1996).
[48] P. E. Blöchl, Phys. Rev. B **50**, 17953 (1994).
[49] J. P. Perdew and A. Zunger, Phys. Rev. B **23**, 5048 (1981).
[50] J. P. Perdew and Y. Wang, Phys. Rev. B **45**, 13244 (1992).
[51] J. P. Perdew, K. Burke, and M. Ernzerhof, Phys. Rev. Lett. **77**, 3865 (1996).
[52] A. Togo, F. Oba, and I. Tanaka, Phys. Rev. B **78**, 134106 (2008).
[53] Q. Hu, D. Sun, Q. Wu, H. Wang, L. Wang, B. Liu, A. Zhou, and J. He, J. Phys. Chem. C **117**, 14253 (2013).
[54] See Supplemental Material at http://link.aps.org/supplemental/10.1103/PhysRevB.94.104103 for the determination of effective thickness of MXene, the in-plane bulk stress-strain curves of Ti_3C_2 and $Ti_3C_2T_2$ (T = Cl, F, H, O, and OH), the phonon dispersion curves for Ti_3C_2 and $Ti_3C_2O_2$, and the calculated density of state for Ti_3AlC_2.
[55] X.-H. Zha, K. Luo, Q. Li, Q. Huang, J. He, X. Wen, and S. Du, Europhys. Lett. **111**, 26007 (2015).
[56] M. Dion, H. Rydberg, E. Schroder, D. C. Langreth, and B. I. Lundqvist, Phys. Rev. Lett. **92**, 246401 (2004).
[57] J. Klimeš, D. R. Bowler, and A. Michaelides, Phys. Rev. B **83**, 195131 (2011).
[58] K. Liu, Q. Yan, M. Chen, W. Fan, Y. Sun, J. Suh, D. Fu, S. Lee, J. Zhou, and S. Tongay, Nano Lett. **14**, 5097 (2014).
[59] C. Si, Z. Liu, W. Duan, and F. Liu, Phys. Rev. Lett. **111**, 196802 (2013).
[60] R. F. Zhang, D. Legut, Z. J. Lin, Y. S. Zhao, H. K. Mao, and S. Veprek, Phys. Rev. Lett. **108**, 255502 (2012).
[61] R. F. Zhang, D. Legut, X. D. Wen, S. Veprek, K. Rajan, T. Lookman, H. K. Mao, and Y. S. Zhao, Phys. Rev. B **90**, 094115 (2014).
[62] R. F. Zhang, D. Legut, Z. H. Fu, S. Veprek, Q. F. Zhang, and H. K. Mao, Phys. Rev. B **92**, 104107 (2015).
[63] E. Konstantinova, S. O. Dantas, and P. M. V. B. Barone, Phys. Rev. B **74**, 035417 (2006).
[64] T. Li, Phys. Rev. B **85**, 235407 (2012).
[65] Q. Wei and X. H. Peng, Appl. Phys. Lett. **104**, 251915 (2014).
[66] A. Enyashin and A. Ivanovskii, Comput. Theor. Chem. **989**, 27 (2012).
[67] M. Topsakal, S. Cahangirov, and S. Ciraci, Appl. Phys. Lett. **96**, 091912 (2010).
[68] T. Shao, B. Wen, R. Melnik, S. Yao, Y. Kawazoe, and Y. Tian, J. Chem. Phys. **137**, 194901 (2012).
[69] X. Wei, B. Fragneaud, C. A. Marianetti, and J. W. Kysar, Phys. Rev. B **80**, 205407 (2009).
[70] G. Kalosakas, N. N. Lathiotakis, C. Galiotis, and K. Papagelis, J. Appl. Phys. **113**, 134307 (2013).
[71] O. Leenaerts, H. Peelaers, A. D. Hernandez-Nieves, B. Partoens, and F. M. Peeters, Phys. Rev. B **82**, 195436 (2010).
[72] P. Wagner, V. V. Ivanovskaya, M. J. Rayson, P. R. Briddon, and C. P. Ewels, J. Phys.: Condens. Mater. **25**, 155302 (2013).
[73] M. T. Dove, *Introduction to lattice dynamics* (Cambridge University Press, Cambridge, 1993), Vol. 4, pp. 95–100.
[74] C. A. Marianetti and H. G. Yevick, Phys. Rev. Lett. **105**, 245502 (2010).
[75] E. B. Isaacs and C. A. Marianetti, Phys. Rev. B **89**, 184111 (2014).
[76] T. Timusk and B. Statt, Rep. Prog. Phys. **62**, 61 (1999).